

Effect of processing parameters on surface roughness, porosity and cracking of as-built IN738LC parts fabricated by laser powder bed fusion

Guo, Chuan; Li, Sheng; Shi, Shi; Li, Xinggang; Hu, Xiaogang; Zhu, Qiang; Ward, R. Mark

DOI:
[10.1016/j.jmatprotec.2020.116788](https://doi.org/10.1016/j.jmatprotec.2020.116788)

License:
Creative Commons: Attribution-NonCommercial-NoDerivs (CC BY-NC-ND)

Document Version
Peer reviewed version

Citation for published version (Harvard):
Guo, C, Li, S, Shi, S, Li, X, Hu, X, Zhu, Q & Ward, RM 2020, 'Effect of processing parameters on surface roughness, porosity and cracking of as-built IN738LC parts fabricated by laser powder bed fusion', *Journal of Materials Processing Technology*, vol. 285, 116788. <https://doi.org/10.1016/j.jmatprotec.2020.116788>

[Link to publication on Research at Birmingham portal](#)

General rights

Unless a licence is specified above, all rights (including copyright and moral rights) in this document are retained by the authors and/or the copyright holders. The express permission of the copyright holder must be obtained for any use of this material other than for purposes permitted by law.

- Users may freely distribute the URL that is used to identify this publication.
- Users may download and/or print one copy of the publication from the University of Birmingham research portal for the purpose of private study or non-commercial research.
- User may use extracts from the document in line with the concept of 'fair dealing' under the Copyright, Designs and Patents Act 1988 (?)
- Users may not further distribute the material nor use it for the purposes of commercial gain.

Where a licence is displayed above, please note the terms and conditions of the licence govern your use of this document.

When citing, please reference the published version.

Take down policy

While the University of Birmingham exercises care and attention in making items available there are rare occasions when an item has been uploaded in error or has been deemed to be commercially or otherwise sensitive.

If you believe that this is the case for this document, please contact UBIRA@lists.bham.ac.uk providing details and we will remove access to the work immediately and investigate.

**Effect of processing parameters on surface roughness, porosity and cracking of
as-built IN738LC parts fabricated by laser powder bed fusion**

**Chuan Guo^{a,b,c}, Sheng Li^c, Shi Shi^d, Xinggang Li^{b,e}, Xiaogang Hu^{a,b}, Qiang
Zhu^{a,b*}, R. Mark Ward^{c,**}**

^a Department of Mechanical and Energy Engineering, Southern University of Science
and Technology, Shenzhen 518055, PR China

^b Shenzhen Key Laboratory for Additive Manufacturing of High-performance materials,
Shenzhen 518055, PR China

^c School of Metallurgy and Materials, University of Birmingham, Edgbaston,
Birmingham B15 2TT, UK

^d Guangdong Provincial Key Laboratory of Durability for Marine Civil Engineering,
Shenzhen Durability Center for Civil Engineering, College of Civil and Transportation
Engineering, Shenzhen University, Shenzhen, 518060, Guangdong, PR China

^e Academy for Advanced Interdisciplinary Studies, Southern University of Science and
Technology, Shenzhen 518055, PR China

*Corresponding author 1: Qiang Zhu

E-mail address: zhuq@sustech.edu.cn

**Corresponding author 2: R. Mark Ward

E-mail address: R.M.Ward@bham.ac.uk

Abstract: An investigation was conducted to understand how different parameters, namely laser power, scan speed and hatch spacing, influence the printing qualities, i.e. surface roughness, porosity and crack density of the nickel-based superalloy Inconel 738LC during laser powder bed fusion. Insufficient overlap, Plateau–Rayleigh instability and Marangoni convection were identified and characterized as the factors that could deteriorate the surface quality of as-built IN738LC parts. Two leading causes of pore were determined by metallographic analysis and computed tomography as lack of fusion and keyhole, which were attributed to different energy input densities. Crack density was measured by metallographic observation. Residual stress and the time for solidification of melt were identified as the key factors that affected the crack density. Finally, the relationships between the printing qualities and volume energy density were established by regression analysis, and the VED of $\sim 48 \text{ J/mm}^3$ was optimal for fabricating IN738LC in the LPBF process

Keywords: Laser powder bed fusion, nickel-based superalloy, processing parameters, surface roughness, porosity, crack density.

1. Introduction

Additive Manufacture (AM), also known as 3D Printing, has attracted wide attention from both engineering and research communities due to the advantages of high design freedom, minimal feedstock waste and less post-machining steps. Laser powder bed fusion (LPBF) is a powder bed AM technique, where the bulk objectives are fabricated directly from metallic powders in a “layer by layer” fashion. Guo et al. (2018) suggested that LPBF had become one of the most dominant techniques in the

metal AM process.

Inconel 738LC (IN738LC) is a high-end nickel-based superalloy with an fcc- γ matrix and mainly strengthened by fine γ' precipitations with $\text{Ni}_3(\text{Al}, \text{Ti})$ chemical composition and L_{12} crystal structure. IN738LC exhibits a high creep and corrosion resistance at elevated temperatures, which enables its wide use in the aerospace field as turbines disc and blades, etc. (Wang et al. (2019)). Recently, the LPBF technique is also applied to process IN738LC in order to meet the high requirement of the complex shape and the design freedom of components. However, the IN738LC alloy has been known as an un-weldable alloy due to its high contents of Ti and Al ($\text{Ti} + \text{Al} > 6 \text{ wt\%}$), indicating that the process window of IN738LC processed by LPBF is too limited to obtain the components without any defects.

Due to the complex fluid dynamics and solidification process of the metallic liquid in melt pool, the objectives processed by LPBF still undergo a problem in terms of high surface roughness. Although the outer layer of printed parts can be machined by post-processing, the surface quality of powder layer can significantly affect the subsequent spreading of powders and further influence the generation of defects during manufacturing. Tian et al. (2017) indicated that the balling effect was the main factor that deteriorated the surface quality of the Hastelloy X parts produced by LPBF. Qiu et al. (2015) directly observed the interaction between laser beam and powder bed. They suggested that the Marangoni force and the recoil pressure were the main reason causing the instability of melt flow, which was responsible for high surface roughness. Mumtaz, Hopkinson (2009) conducted a single scanning experiment on the Inconel 625

parts with different parameters. And they remarked that a relatively high peak power aided a reduction in surface roughness for both top and side surfaces of the printed parts due to the improved wettability of melt pool. Pore is also susceptible to the processing parameters in the LPBF process. Cloots et al. (2016) found two types of pores i.e. spherical pore and bonding defects in the IN738LC parts manufactured by LPBF and they thought that the scan speed of 900 mm/s was an inflection point between low and high porosity. However, when energy input density (laser power/scan speed) exceeded a specific value, another type of pore appeared accompanying with keyhole in the research of Guraya et al. (2019) when they processed IN738LC using LPBF. Among the defects in IN738LC, cracking is the most serious due to its bad effect on mechanical properties. The processing parameters can significantly affect the cracking in the LPBF process. Cloots et al. (2016) suggested that increasing scan speed could decrease the crack density of IN738LC in both Gaussian and doughnut profile of the laser beam. Chen et al. (2016) had a similar finding in laser additive manufactured Inconel 718. Wang et al. (2019) applied a large range of laser powers and scan speeds on the IN738LC alloy fabricated by LPBF. They found that a number of process parameters could yield the parts with a large amount of cracking and some of them even failed to be built in terms of wrapping.

LPBF parameters like laser power, scan speed and hatch spacing can significantly affect the printing behaviors and further affect the mechanical properties of printed components. In order to obtain the parts with excellent qualities, it is essential to understand the influence of these parameters on the formation of defects and their action

mechanisms. In the present work, the printing qualities of IN738LC manufactured by LPBF, i.e. surface, pore and crack were investigated by a single variable method to find the formation mechanism of these defects with different laser powers, scan speeds and hatch spacings as an approach towards eliminating them. The results would be also helpful to understand the fluid dynamics and the solidification behavior of melt pool in the LPBF process.

2. Experimental procedure

2.1. IN738LC powder

The IN738LC powder used in the present investigation were provided by gas atomization in an argon atmosphere from LPW Technology Ltd (UK). Particle distribution was measured by a laser particle size analyzer (LPA) and the D-values were $D_{10} = 27.6 \mu\text{m}$, $D_{50} = 39.1 \mu\text{m}$ and $D_{90} = 49.3 \mu\text{m}$. The chemical composition of the powder is listed in Table 1. A Hitachi TM3000 scanning electron microscope (SEM) was performed to observe the morphology of the powders, as shown in Fig. 1.

Ni	Co	Cr	W	Ta	Ti	Al	Mo	Nb	Zr	B	C
Bal.	8.44	15.9	2.57	1.73	3.33	3.4	1.81	0.88	0.04	0.01	0.11

Table 1 Chemical composition of the IN738LC powder (wt%).

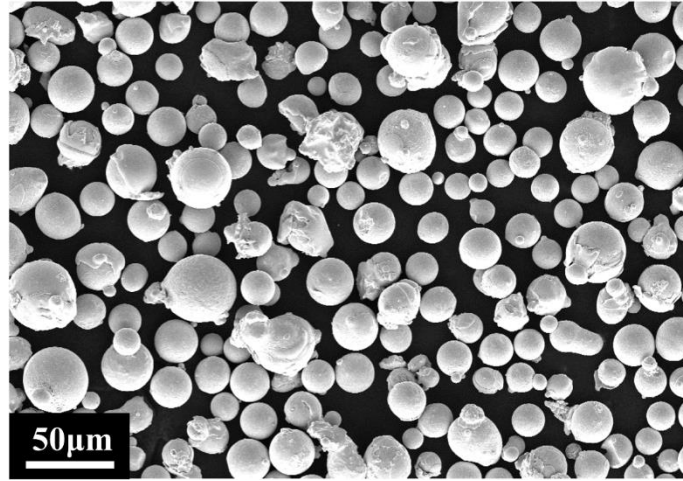


Fig. 1. SEM image of the IN738LC powders.

2.2. LPBF process

The LPBF process was conducted by a Concept Laser M2 Cusing system equipped with a 400 W continuous-wave fiber laser and the maximum scan speed could reach 4200 mm/s. An experiment with the single variable method was designed among these three key parameters (hatch spacing, scan speed and laser power), where the primary parameter increased in gradient while the other two were fixed. However, it was challenging to measure the crack density on the samples with high porosity in the current experimental condition. On the one hand, pores might hide the presence of cracks on polished surfaces. On the other hand, the stress that caused cracking would be relieved to some extent through pores. These could weaken the responsivity of the parameters on the crack density, implying that the porosity needed to be strictly controlled in the samples for the study of cracks. Thus, two series of parameters were applied for the investigations of porosity (surface roughness) and crack density, as given in Table 2 and Table 3, respectively. The thickness of layer was fixed as 30 μm and the scan strategy was 90° raster, i.e. the scan direction was uniform in a layer and rotated

90° between layers, as shown in Fig. 2a. The samples were built into cubes with the dimensions of 10 mm × 10 mm × 10 mm for metallographic observation and 50 mm × 15 mm × 15 mm for tensile testing. Furthermore, the samples for the study of cracks were annealing treated together with the substrate at 840 °C for 24 h (Messé et al. (2018)) in order to relieve the stress, avoiding the formation of new cracks after cutting from the substrate.

Sample	Laser power (W)	Scan speed (mm/s)	Hatch spacing (μm)	Volume energy density (J/mm^3)
1	200	2000	30	111.11
2	200	2000	45	74.07
3	200	2000	60	55.56
4	200	2000	75	44.44
5	200	2000	90	37.04
6	200	1000	75	88.89
7	200	1500	75	59.26
8	200	2000	75	44.44
9	200	2500	75	35.56
10	200	3000	75	29.63
11	150	2000	90	27.78
12	200	2000	90	37.04
13	250	2000	90	46.30
14	300	2000	90	55.56
15	350	2000	90	64.81

Table 2 Processing parameters for the analysis of the surface roughness and the porosity.

Sample	Laser power (W)	Scan speed (mm/s)	Hatch spacing (μm)	Volume energy density (J/mm^3)
1	250	2000	50	83.33
2	250	2000	60	69.44
3	250	2000	70	59.52
4	250	2000	80	52.08
5	200	1500	60	74.07
6	200	1750	60	63.49
7	200	2000	60	55.56
8	200	2250	60	49.38
9	175	2000	60	48.61
10	200	2000	60	55.56
11	225	2000	60	62.50
12	250	2000	60	69.44

Table 3 Process parameters for the analysis of the crack density.

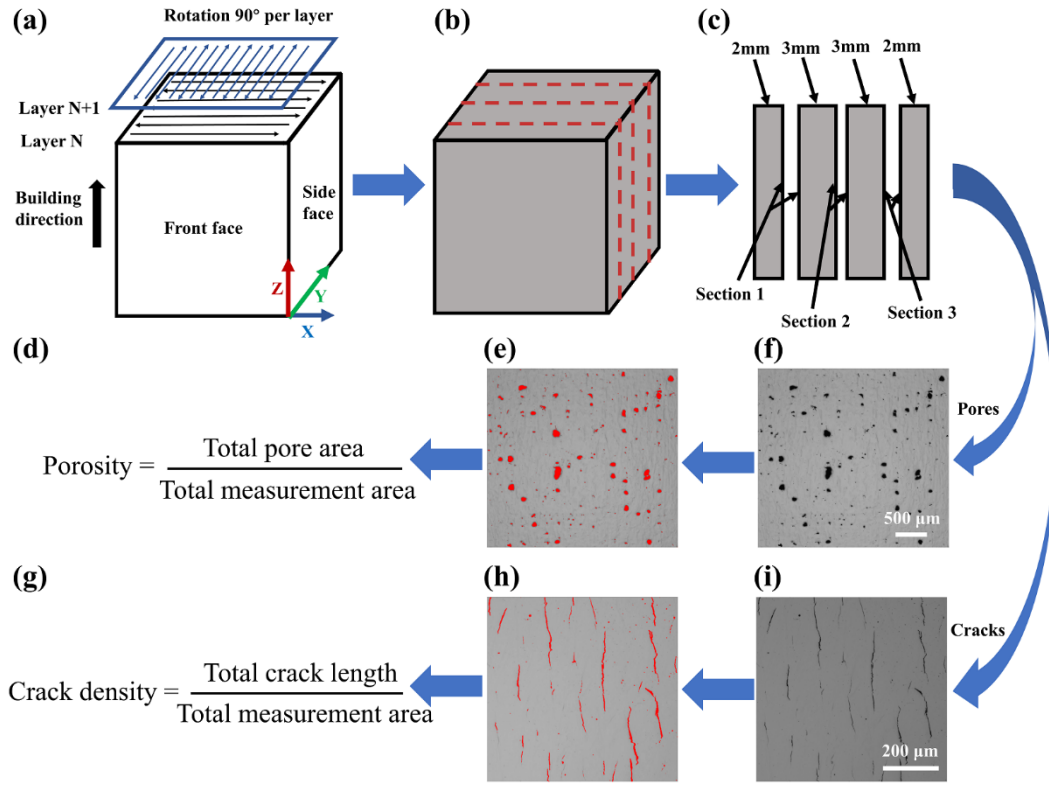


Fig. 2. (a) Schematic representation of the 90° raster scan strategy, (b,c) schematic representation of the sample cutting method, (d-f) analysis procedure for the porosity, (g-i) analysis procedure for the crack density.

2.3. Analysis procedure

To measure the surface roughness, top surfaces of the samples were scanned by a laser scan confocal microscope (LSCM) from OLYMPUS LEXT. The surface roughness was determined by averaging nine different scanning areas with the dimensions of 1280 μm × 960 μm. Morphology of the surfaces was observed by a PHILIPS XL-30 SEM. The samples were cut parallel to the building direction into three sections by a wire electro-discharge machining (EDM) for the porosity and crack density measurements, as shown in Fig. 2b and Fig. 2c. These sections were ground sequentially by 400 CW, 600 CW, 1000 CW, 1500 CW abrasive paper and then polished down by 0.04 μm colloidal silica suspension. The measurements were conducted using

Image J from optical microscopic (OM) observation and the procedure is depicted in Fig. d-i. Porosity was the ratio of the total area of pores to the total measurement area. Crack density was measured in terms of Fig. 2h, where the cracks were identified by the image threshold technics. The length of each crack was measured and added together, and the result was the ratio of the total length of cracks to the total measurement area. The reported porosity and crack density were averaged from five different images taken in each section. Details of pores were observed by the Hitachi TM3000 SEM. 3D characterization of pores was performed by a diando d2 computed tomography (CT) system with the samples in the dimensions of 3 mm \times 3 mm \times 3 mm. In the CT testing, the monochromatic beam volt and current were 120 kV and 90 μ A, respectively with a resolution ratio of 2 μ m/pixel. 2040 tomograms reconstruction and data collection were operated by diControl and VG Studio software.

2.4. Tensile testing

Tensile testing was conducted under a strain rate of 2 mm/min by a ZJSY RDL100 tensile testing machine at room temperature for the samples perpendicular to the building direction. The reported data were the average of five tests. All the samples were annealing treated before testing in order to avoid the formation of new cracks after cutting from the substrate and ensure that the defects were the only factor affecting the mechanical properties.

3. Results and discussion

3.1. Surface roughness

3.1.1. Effect of hatch spacing

Fig. 3a shows the surface roughness (R_a) as a function of the hatch spacing. It can be seen that the surface roughness increased with increasing the hatch spacing in case that the hatch spacing was larger than $45\text{ }\mu\text{m}$. The highest surface roughness was $21.1\text{ }\mu\text{m}$ at the hatch spacing of $90\text{ }\mu\text{m}$, while the lowest value was $11.16\text{ }\mu\text{m}$ when the hatch spacing was $45\text{ }\mu\text{m}$. However, the surface roughness at the lowest hatch spacing ($30\text{ }\mu\text{m}$) was higher than that at $45\text{ }\mu\text{m}$.

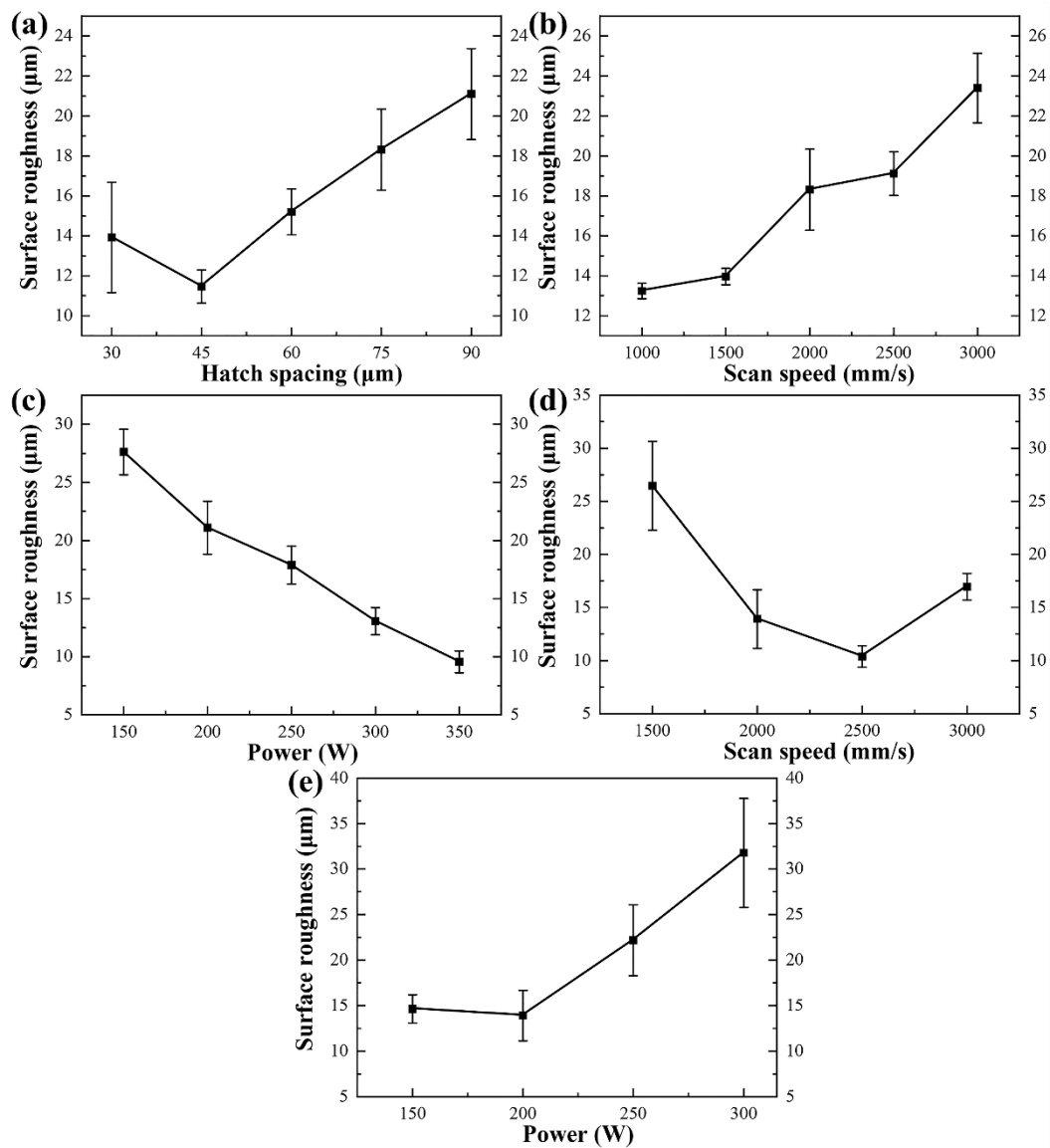


Fig. 3. Surface roughness as a function of (a) the hatch spacing (laser power 200 W, scan speed 2000 mm/s), (b) the scan speed (laser power 200 W, hatch spacing $75\text{ }\mu\text{m}$),

(c) the laser power (scan speed 2000 mm/s, hatch spacing 90 μm), (d) the scan speed (laser power 200 W, hatch spacing 30 μm) and (e) the laser power (scan speed 2000 mm/s, hatch spacing 30 μm).

The SEM and reconstruction images of the top surfaces are shown in Fig.4. Big gaps between the adjacent laser tracks were observed when the hatch spacing was high, as shown in Fig. 4e. The corresponding reconstruction image (Fig. 4f) shows a large height difference between the top and the bottom of the tracks, which directly resulted in high surface roughness. On the contrary, when the hatch spacing was low, sufficient overlaps between the tracks was favorable to form a relatively flat surface, as shown in Fig. 4c. Nevertheless, when the hatch spacing continued reducing to 30 μm , the surface roughness increased to 13.92 μm with a large deviation. It can be explained by the humping phenomenon due to the Marangoni flow as a considerably low hatch spacing is applied in the LPBF process. The schematic for illustrating the transfer of melt between the tracks with different hatch spacings is revealed in Fig. 5. In the study of Rombouts et al. (2006) and Zhou et al. (2015), they held the idea that the Marangoni convection occurred when melt flowed from the regions with low surface tension to the region with high surface tension in melt pool. Typically, surface tension is inversely related to temperature, implying a high temperature favors a low surface tension. The temperature in the center of melt pool is normally higher than that located on the edge. Therefore, the direction of the attendant Marangoni flow is from the center to the edge, which results in a mass transfer of melt from the present track to the previously fabricated tracks. When the hatch spacing is relatively large, the melt transferred by the

Marangoni flow can fill in the gaps between the tracks, which contributes to a flat surface, as shown in Fig. 5a. Tan et al. (2018) found a clear trace of the Marangoni flow at the bottom of the melt pool in the steel-copper functional bimetal produced by LPBF since the high thermal conductivity of copper increased the temperature gradient, by which the Marangoni flow was enhanced. The temperature gradient between tracks increases at a low hatch spacing, which is proven by Xia et al. (2016) using the simulation method, thus increasing the trend of the Marangoni flow. In addition, a low hatch spacing can increase thermal accumulation and a relatively high working temperature is obtained in melt pool. The high temperature tends to reduce the viscosity of melt, which is beneficial for the Marangoni flow. Therefore, the vigorous Marangoni flow increases the intensity of the mass transfer to the previously fabricated tracks at a considerably low scan spacing, inducing a stacking of material on the top surface of the tracks, and then the micro-humping occurs after solidification, as shown in Fig. 5b. Fig. 4a and b show the micro-humping phenomenon by SEM and LSCM (red dotted line).

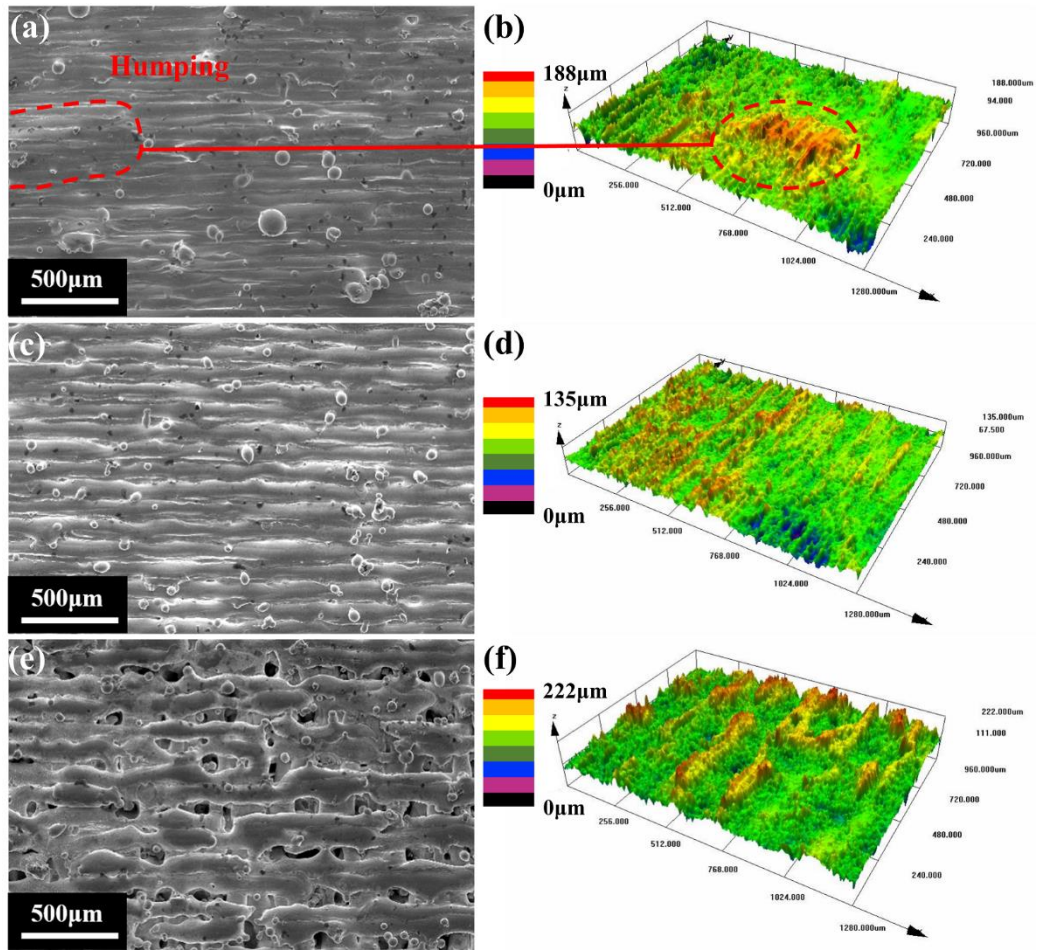


Fig. 4. SEM and reconstruction images of the top surfaces at the hatch spacings of (a,b) 30 μm , (c,d) 45 μm and (e,f) 90 μm (laser power 200 W, scan speed 2000 mm/s).

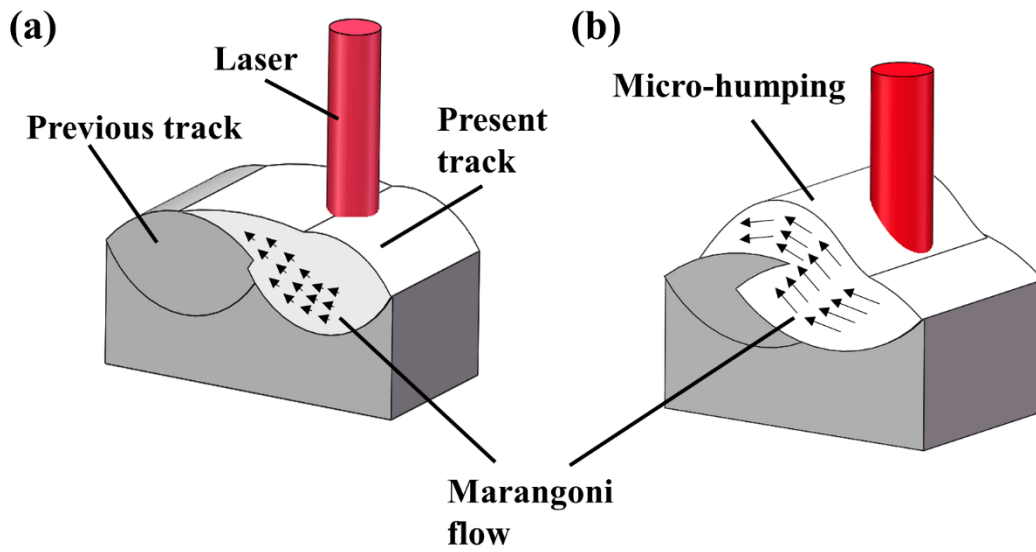


Fig. 5. Illustrations of the mass transfer between the tracks at (a) the high hatch spacing, and (b) the low hatch spacing.

3.1.2. Effect of scan speed

Fig. 3b shows the surface roughness as a function of the scan speed. The surface roughness had a clear increasing trend with the increase of the scan speed. The scan speed of 1000 mm/s corresponded to a minimum roughness and the surface roughness was 13.24 μm .

When the scan speed is low, the high energy input density (laser power/scan speed) induces the powders to fully melt, which is beneficial for the formation of a flat surface, indicated by the SEM and reconstruction images of the top surface in Fig. 6a and b. As the scan speed increased to 2000 mm/s, the tracks began to swell and clear gaps between the tracks could be seen, as shown in Fig. 6d. When the scan speed reached 3000 mm/s, the tracks became fluctuant and irregular-shaped, suggesting that an unstable condition occurred. In this instance, from Fig. 6e, the discontinuity and the instability of the track made it difficult to recognize the scan direction of the laser beam. The Plateau-Rayleigh instability contributes to this unstable condition when a considerably high scan speed is applied in LPBF. Scipioni et al. (2017) and Li et al. (2017) thought that a molten track could be regarded as a liquid cylinder during the reaction between the laser beam and the powder bed. λ is the length of the cylinder, and D is the diameter. The instability occurs when the ratio of λ to D is larger than π , as shown in Fig. 7a. Yadroitsev et al. (2010) thought that the stability of melt was related to the contact angle θ between the liquid cylinder and the substrate. They suggested that the track trended to stay stable if $\theta < \pi/2$. While in the LPBF process, the top layer is scanned based on the previously fabricated layers, thus, $\theta < \pi/2$ is difficult to sustain. Swell and shrinkage tend to result

in the necking down, inducing the fluctuation of the tracks, as shown in Fig. 7b. As a result, the liquid cylinder trends to break up into small droplets in order to lower the surface energy, known as the balling phenomenon in LPBF. Rayleigh (2010) found that the break time reached its minimum when $\pi D/\lambda = 0.697$ and the time was:

$$t = \{0.3433 \cdot \sqrt{\gamma_{LV} / [\rho \cdot (D/2)^3]}\}^{-1} \quad (1)$$

where γ_{LV} is the surface tension and ρ is the melt density. When D is 100 μm , γ_{LV} is 1.88 N/m, ρ is 7324 kg/m^3 for IN738LC according to the study of Quested et al. (2013), the break time is $\sim 65 \mu\text{s}$. Rombouts et al. (2006) thought that this time was well below the typical solidification time in the LPBF process. In this instance, the breaking up of tracks happened before it solidified, implying the occurrence of the balling phenomenon. They also found that the increase of scan speed led to an increase of the melt pool size and this increase was mainly caused by the pool length, which accordingly increased the ratio of λ to D . Therefore, the high scan speed increases the possibility of the presence of the Plateau–Rayleigh instability.

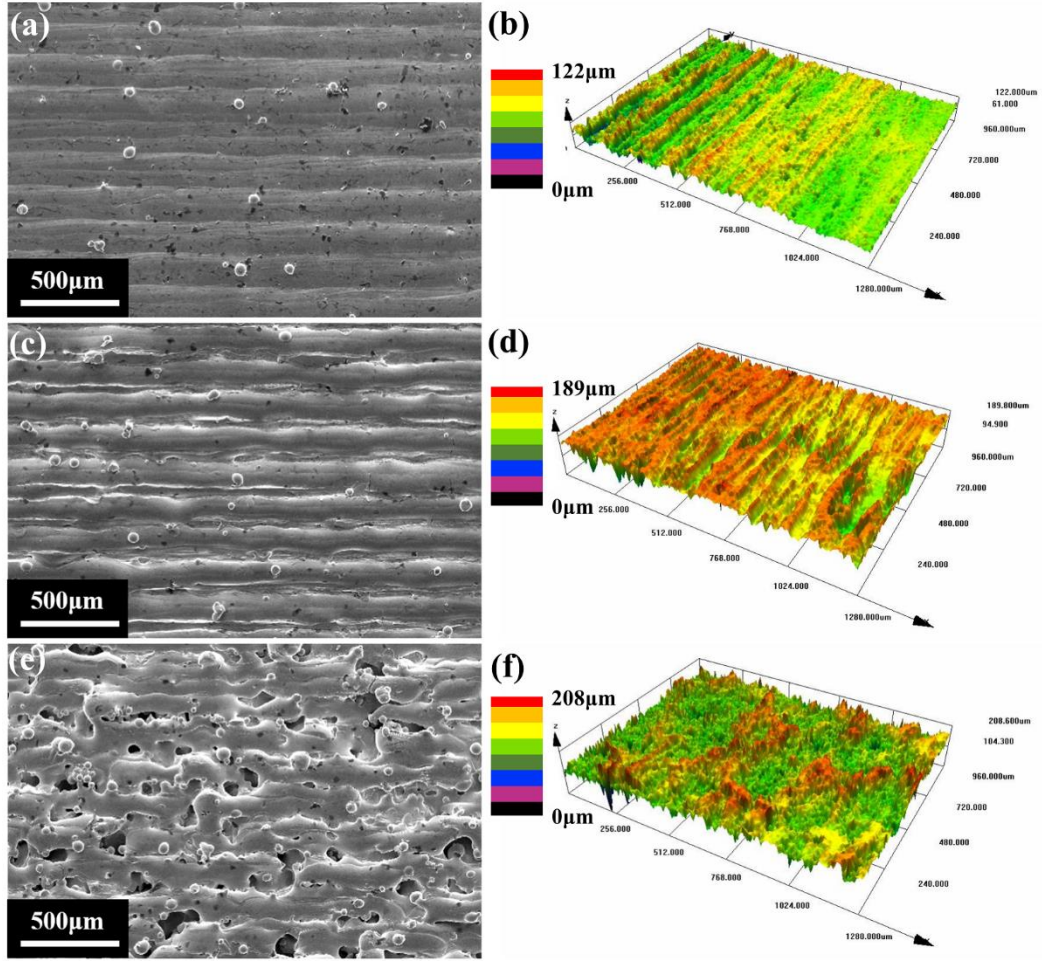


Fig. 6. SEM and reconstruction images of the top surfaces at the scan speed of (a,b) 1000 mm/s, (c,d) 2000 mm/s and (e,f) 3000 mm/s (laser power 200 W, hatch spacing 75 μm).

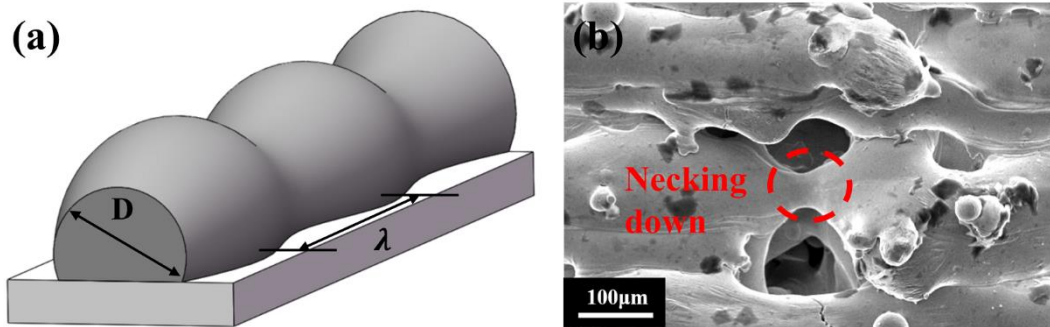


Fig. 7. (a) Illustration of the disturbance of the liquid cylinder, (c) SEM image of the fluctuation of the track, showing the necking down occurs at the scan speed of 3000 mm/s (laser power 200 W and hatch spacing 75 μm).

Fig. 8 shows the top surface with the different scan speeds at high magnification. As the scan speed increased, more and more pores appeared. From Fig. 8a and b, at the scan speed of 1000 mm/s and 1500 mm/s, the surface exhibited free of any pore. However, from Fig. 8d and e, as the scan speed continued increasing to 2500 mm/s and 3000 mm/s, the number of pores increased gradually, which was attributed to the uneven spread of powders and the open pores. The low flowability limits the melt to spread and wet the neighboring tracks fully during the rapid cooling process at a highly applied scan speed in LPBF, thus causing the open pores. As mentioned earlier, viscosity is temperature-dependent, high scan speed tends to lower the working temperature and increase the viscosity of melt during solidification. The melt with high viscosity is less likely to migrate toward the adjacent tracks. After solidification and shrinkage, the open pores are formed, as shown in Fig. 8e. Xia et al. (2017) also observed that the number of open pores increased with increasing the scan speed during the LPBF of Inconel 718. Khairallah et al. (2016) thought that open pores were formed after the laser beam passed through the present location and accompanying with the increase of surface tension, the pores kept opening due to the depression by the recoil force. Furthermore, a large number of un-melted particles caused by the lack of fusion can be observed at the scan speed of 3000 mm/s, as shown in Fig. 8f.

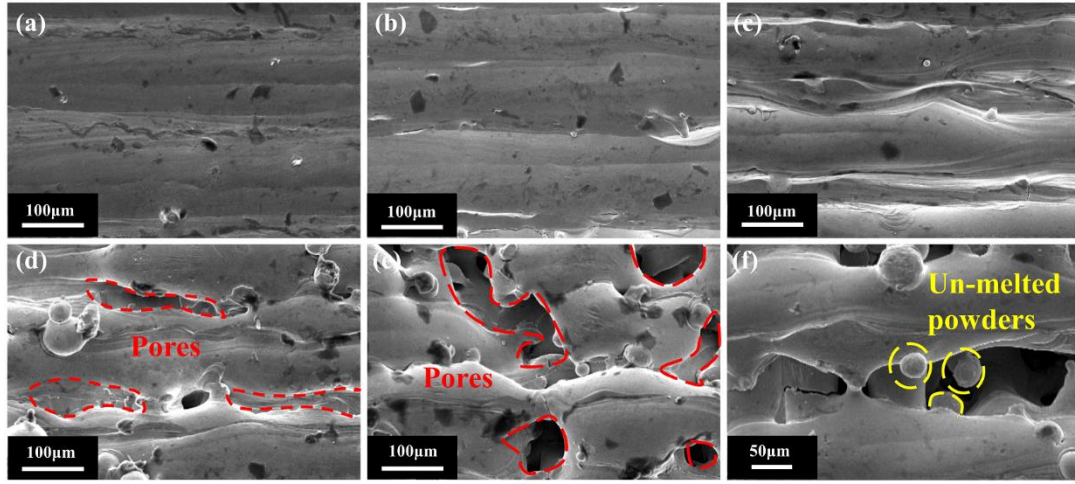


Fig. 8. SEM images at high magnification of the top surfaces at the scan speed of (a) 1000 mm/s, (b) 1500 mm/s, (c) 2000 mm/s, (d) 2500 mm/s, (e, f) 3000 mm/s (laser power 200 W, hatch spacing 75 μm).

Due to the abnormal condition related to the micro-humping phenomenon when a low hatch spacing was applied, the surface roughness as a function of the scan speed was investigated at the hatch spacing of 30 μm , as shown in Table 4. The results are in Fig. 3d. Similarly, high scan speed (3000 mm/s) deteriorated the surface quality and the corresponding surface roughness was 16.96 μm . It was better than that when the hatch spacing was 75 μm (the surface roughness was 23.4 μm) since the overlap was improved at a low hatch spacing. However, it is evident that the lowest surface roughness was attained at the scan speed of 2500 mm/s, and the micro-humping occurred with a continuous reduction of scan speed, inducing high surface roughness at 2000 mm/s and 1500 mm/s. It is worth noting that macro-humping could be seen when the scan speed was 1000 mm/s, as shown in Fig. 9a. In this instance, the solidified materials exhibited as an irregular wave-morphology on the top surface due to the accumulation of violent mass transfer and the instability of melt, which exceeded the

measurement of surface roughness using LSCM. Low scan speed will increase the time interval between tracks and relevantly promote the heat transfer from the present track to previously solidified material, which could increase the thermal gradient between tracks and further enhance the intensity of humping. Furthermore, the melt with low viscosity induced by low scan speed also favors aggravating the mass migration of melt.

Sample	Laser power (W)	Scan speed (mm/s)	Hatch spacing (μm)	Volume energy density (J/mm^3)
1	200	1000	30	222.22
2	200	1500	30	148.15
3	200	2000	30	111.11
4	200	2500	30	88.89
5	200	3000	30	74.07

Table 4 Processing parameters for the analysis of the relationship between the surface roughness and the scan speed at the hatch spacing of 30 μm .

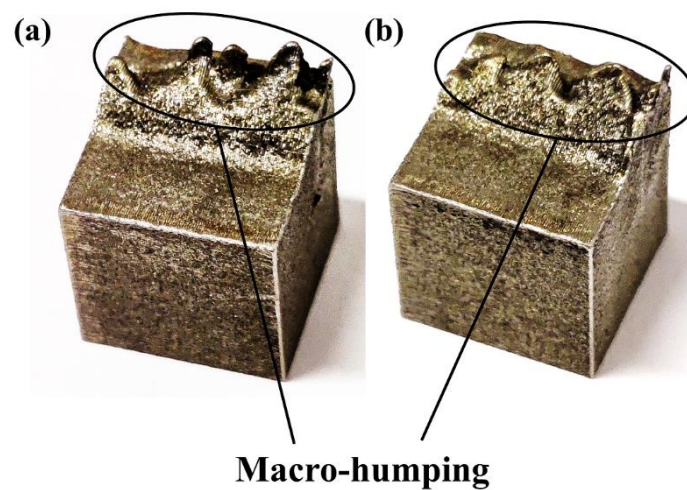


Fig. 9. Images of the macro-humping phenomenon on the top surfaces of the samples with the parameters of (a) hatch spacing 30 μm , laser power 200 W, scan speed 1000

mm/s and (b) hatch spacing 30 μm , laser power 350 W, scan speed 2000 mm/s.

3.1.3. Effect of laser power

Fig. 3c illustrates a linear drop in the surface roughness with increasing the laser power from 150 W to 350 W. Big gaps were formed between the tracks due to the lack of overlap at the laser power of 150 W, as shown in Fig. 10a. Although the tracks kept stable along the laser scanning direction, the big gaps between the tracks and the intermittent discontinuity tended to induce a poor surface quality. When the laser power increased to 250 W, in contrast, the top surface became flat due to the sufficient overlap with an efficient metallurgical bond between the tracks. However, some pores can still be observed between the tracks, as shown in Fig. 10c. Meanwhile, the discontinuity phenomenon disappeared. Continuous elevating the laser power to 350 W, a high-quality surface was obtained (Fig. 10e and f).

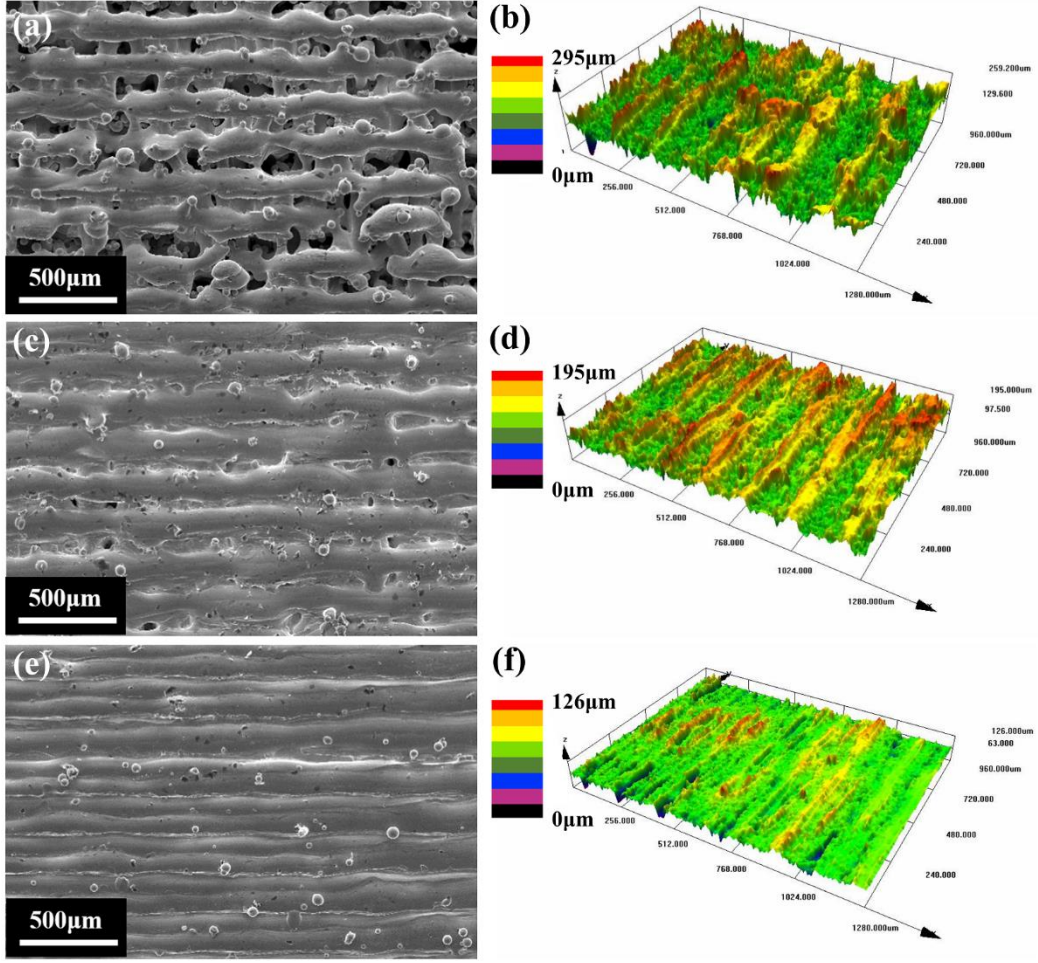


Fig. 10. SEM and reconstruction images of the top surfaces at the laser power of (a,b) 150 W, (c,d) 250 W and (e,f) 350 W (scan speed 2000 mm/s, hatch spacing 90 μm).

In addition, another type of balling was observed when the laser power was as high as 250 W and 300 W, as shown in Fig. 11b. This type of balling phenomenon is ascribed to the reverse flow direction of the Marangoni convection. As it is mentioned, normally, the direction of the Marangoni convection is from the center of melt pool to the edge, which induces a considerable amount of melt to flow towards the neighboring tracks. However, some elements with high surface activity characteristics can significantly reduce the surface tension of melt, which further changes the sign of the gradient of surface tension to temperature and the Marangoni convection is accordingly dragged

from the edge of melt pool to the center. A large amount of melt comes together and an agglomeration of material is formed, which exhibits as a ball morphology on the top of the melt pool after solidification, as illustrated in Fig. 11a. Rombouts et al. (2006) and Zhou et al. (2015) found that sulfur and oxygen were the key elements that could induce the balling phenomenon. Li, Gu (2014) thought that the temperature gradient increased significantly at high laser power, which could induce a high gradient of surface tension along the building direction and enhance the Marangoni convection. Therefore, this type of balling is more likely to occur at high laser power. When the laser power reached its maximum value, i.e. 350 W, however, no balling was formed, as shown in Fig. 10e. It is primarily attributed to that a high peak temperature induced by the considerably high laser power results in the intensive evaporation in melt pool, which can promote the recoil pressure. As indicated by Mumtaz, Hopkinson (2009), a strong recoil pressure had the function to detach balls from the solidifying melt pool. Kruth et al. (2004) also thought that the application of high laser power could reduce the trend for the melt pool to undergo the balling phenomenon.

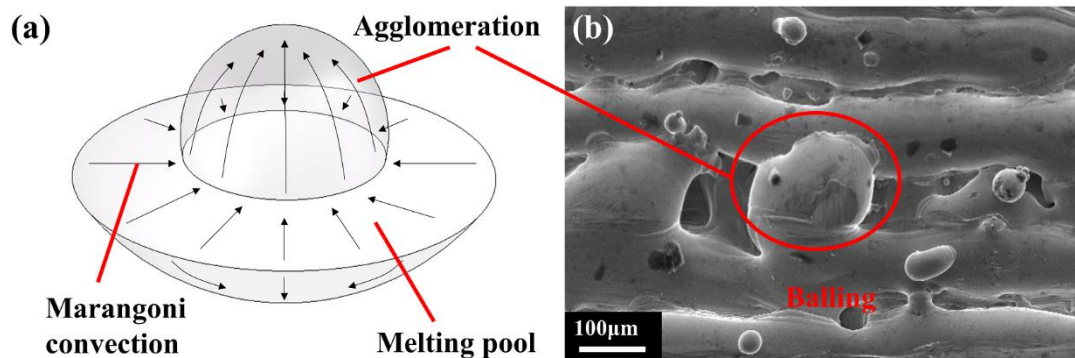


Fig. 11. (a) Illustration of the mechanism of the balling induced by the Marangoni convection, (b) SEM image of a balling morphology at the laser power of 250 W

(scan speed 2000 mm/s, hatch spacing 90 μm).

Similarly, the surface roughness was studied with different laser powers at the hatch spacing of 30 μm , and the parameters are listed in Table 5. The surface roughness as a function of the laser power is shown in Fig. 3e. Although the humping phenomenon was found at 200 W, the incomplete melting induced by low laser power (150 W) led to a worse surface quality than that at 200 W. The surface roughness decreased from 14.64 μm to 13.92 μm when the laser power increased from 150 W to 200 W. The humping effect became more obvious at 250 W and 300 W, and the corresponding surface roughness increased to 22.19 μm and 31.78 μm , respectively. Fig. 9b shows the macro-humping on the sample with the laser power of 350 W. The violent mass transfer related to high laser power was primarily ascribed to the high thermal gradient between tracks (Li, Gu (2014)) and the low-viscosity melt induced by high energy input density.

Sample	Laser power (W)	Scan speed (mm/s)	Hatch spacing (μm)	Volume energy density (J/mm^3)
1	150	2000	30	83.33
2	200	2000	30	111.11
3	250	2000	30	138.89
4	300	2000	30	166.67
5	350	2000	30	194.44

Table 5 Processing parameters for the analysis of the relationship between the surface roughness and the laser power at the hatch spacing of 30 μm .

3.2. Porosity

3.2.1. Effect of hatch spacing

Fig. 12 shows the porosity as a function of the hatch spacing. It can be seen that the porosity increased gradually from 0.1% to 1.11% with the hatch spacing increased from 45 μm to 75 μm and rapidly up to 11.47% at the hatch spacing of 90 μm . The high porosity at the hatch spacing of 90 μm is due to the insufficient overlap between the laser tracks, as shown in Fig. 4e. Un-melted powders due to the lack of fusion were trapped in these irregular-shaped pores, as shown in Fig. 13. Interestingly, the porosity obviously increased to 5.18% with a large deviation at the hatch spacing of 30 μm . It is primarily attributed to the micro-humping phenomenon, which causes the powder layer to be unevenly spread on the previously fabricated layers. When the layer is too thick for the laser beam to penetrate, the pores are correspondingly formed due to the incomplete bond between layers. Besides, Qiu et al. (2015) suggested that a thick layer increased the instability of the melt pool and resulted in the discontinuity of tracks and more spatter. The uneven thickness of the powder layer accumulates as the LPBF process continues due to the contingency of micro-humping. Therefore, the maldistribution of pores tended to appear on the polished surface, indicating a large data deviation in Fig. 12a.

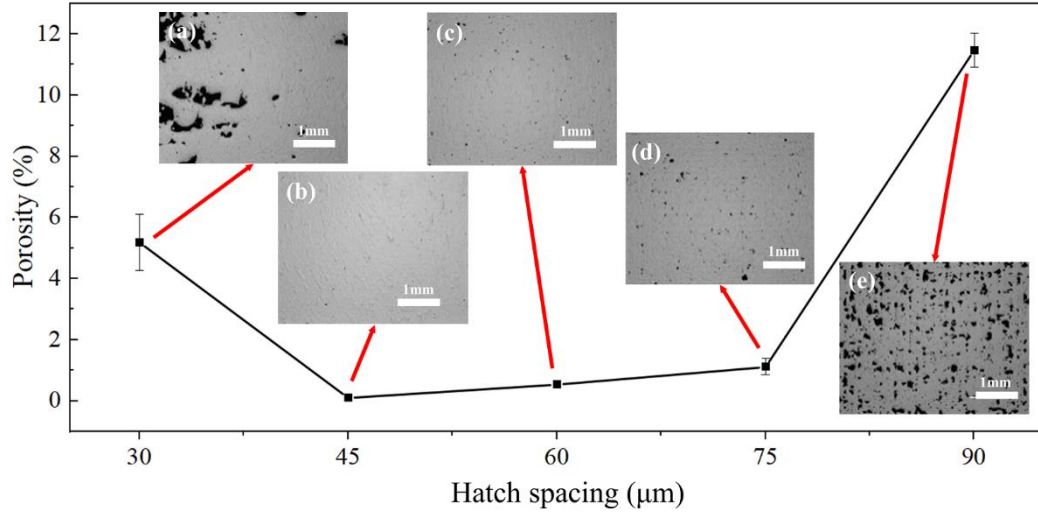


Fig. 12. Porosity as a function of the hatch spacing, inserted OM images show the polished surfaces at hatch spacings of (a) 30 μm , (b) 45 μm , (c) 60 μm , (d) 75 μm and (e) 90 μm (laser power 200 W, scan speed 2000 mm/s).

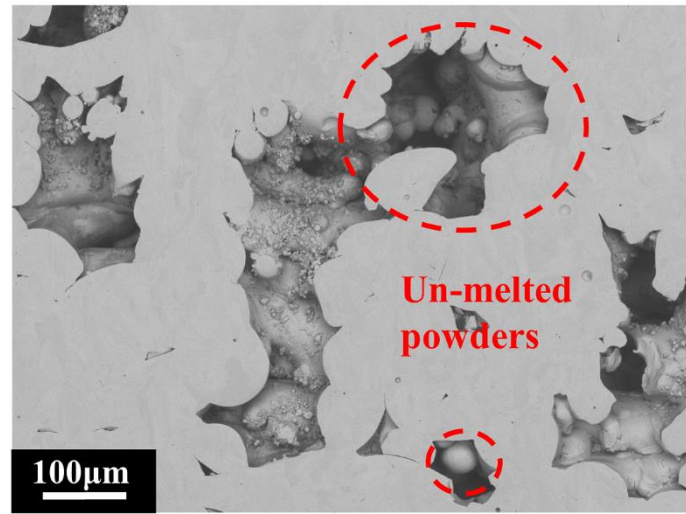


Fig. 13. SEM image of the polished surface showing the un-melted powders at the hatch spacing of 90 μm (laser power 200 W, scan speed 2000 mm/s).

3.2.2. Effect of scan speed

The porosity as a function of the scan speed is shown in Fig. 14. It is apparent that both high and low scan speeds could result in high porosity. When the scan speed was 1000 mm/s, the corresponding porosity was 3.07%, which was higher than that at the

scan speed of 1500 mm/s. As the scan speed increased from 1500 mm/s to 3000 mm/s, the porosity increased from 0.054% to 13.12%. The lack of fusion induced by the high scan speed is the primary cause of the high porosity, as shown in Fig. 15a. The Plateau-Rayleigh instability can be also observed at the scan speed of 3000 mm/s, as shown in Fig. 15b. The fluctuation causes wave crests and wave troughs along the laser scan direction. When the two wave crests overlap together, a bridge-like structure with a dense metallurgical bond is formed. Whilst when the two wave troughs encounter, a big gap appears as a pocket with a large number of un-melted powders trapping in it. The insert image of Fig. 15b illustrates this process.

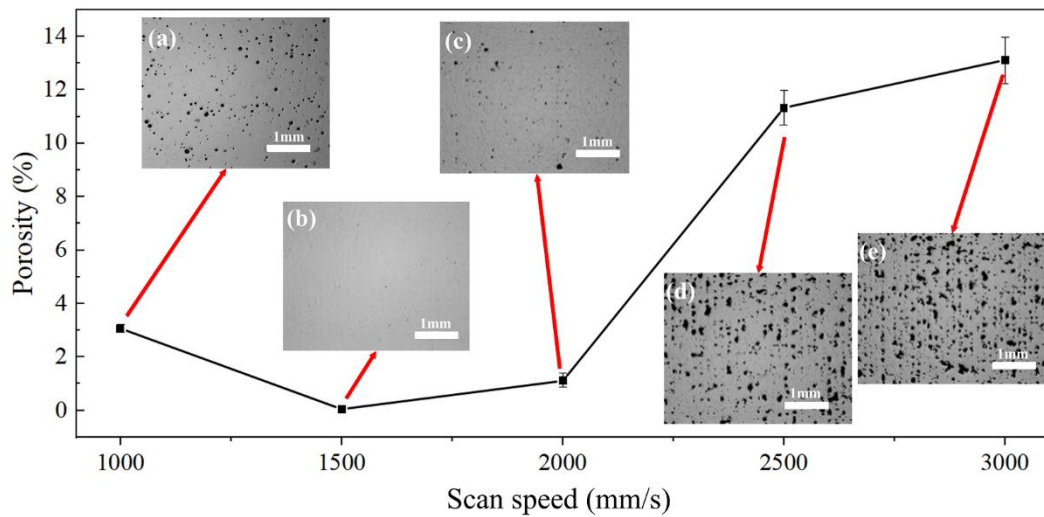


Fig. 14. Porosity as a function of the scan speed, inserted OM images show the polished surfaces at the scan speed of (a) 1000 mm/s, (b) 1500 mm/s, (c) 2000 mm/s, (d) 2500 mm/s and (e) 3000 mm/s (laser power 200 W, hatch spacing 75 μ m).

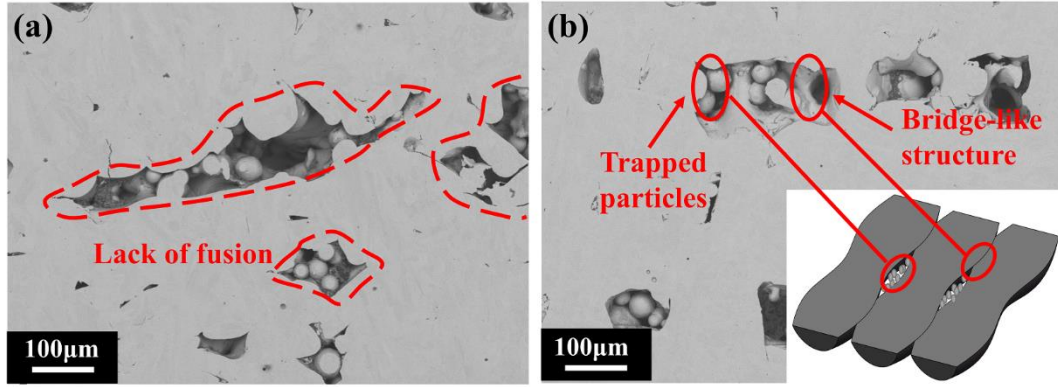


Fig. 15. SEM images of the polished surfaces showing (a) the lack of fusion and (b) bridge-like structure and trapping un-melted powders due to the Plateau–Rayleigh instability at the scan speed of 3000mm/s (laser power 200W, hatch spacing 75µm).

Low scan speed was also favorable to increase the porosity due to another type of pore, i.e. keyhole pore. When the combination of scan speed, laser power and laser beam size exceeds a critical value, the normal conduction mode is possible to transfer to the keyhole mode since the energy input density is high enough to induce evaporation and plasma, which effectively “drill” a deeper depth to form a cavity in melt pool. King et al. (2014) and Fabbro (2010) observed similar behavior in LPBF and welding process. According to Kasperovich et al. (2016), the keyhole pores were formed due to the gas entrapping and the collapse of these cavities with a more rounded shape, as shown in Fig. 14a. An example of the keyhole pore is shown in Fig. 16.

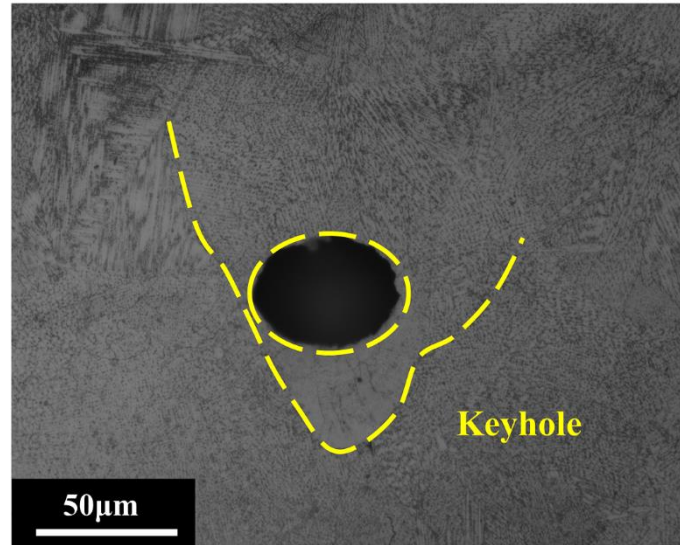


Fig. 16. OM images showing a keyhole pore at the scan speed of 1000 mm/s (laser power 200 W, hatch spacing 75 μm).

3.2.3. Effect of laser power

Fig. 17 shows a disproportionate decrease of the porosity with the increase of the laser power. The maximum porosity was 14.84% at the laser power of 150 W and decreased to 11.47% as the laser power increased to 200 W. The porosity dropped significantly below 1% with continuously increasing the laser power. Similarly, the energy input density accordingly decreases with decreasing the laser power, leading to the lack of fusion and further increasing the porosity.

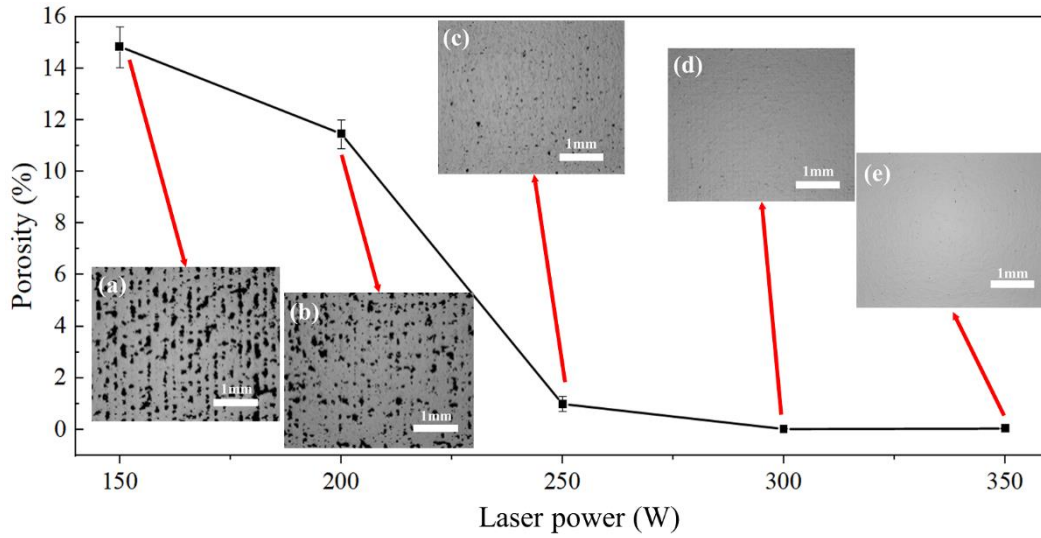


Fig. 17. Porosity as a function of the laser power, insert OM images show the polished surfaces at the laser powers of (a) 150 W, (b) 200 W, (c) 250 W, (d) 300 W and (e) 350 W (scan speed 2000 mm/s, hatch spacing 90 μm).

3.2.4. Effect of volume energy density

Volume energy density (VED) is widely used to justify the comprehensive effect of processing parameters on printing qualities in LPBF. According to the study of Kasperovich et al. (2016), the VED (ψ) is defined as:

$$\psi = \frac{P}{v \cdot h \cdot \xi} \quad (2)$$

where P is the laser power, v is the scan speed, h is the hatch spacing and ξ is the layer thickness. The porosity as a function of the VED is given in Fig. 18b, showing that the minimum porosity was obtained at the VED between $\sim 55 \text{ J/mm}^3$ and $\sim 75 \text{ J/mm}^3$. When the VED increased from $\sim 25 \text{ J/mm}^3$ to $\sim 60 \text{ J/mm}^3$, the porosity decreased from $\sim 15\%$ to $\sim 0.02\%$, while when the VED increased further up, the porosity increased to $\sim 3\%$ and $\sim 5\%$ at the VED $\sim 90 \text{ J/mm}^3$ and $\sim 110 \text{ J/mm}^3$, respectively.

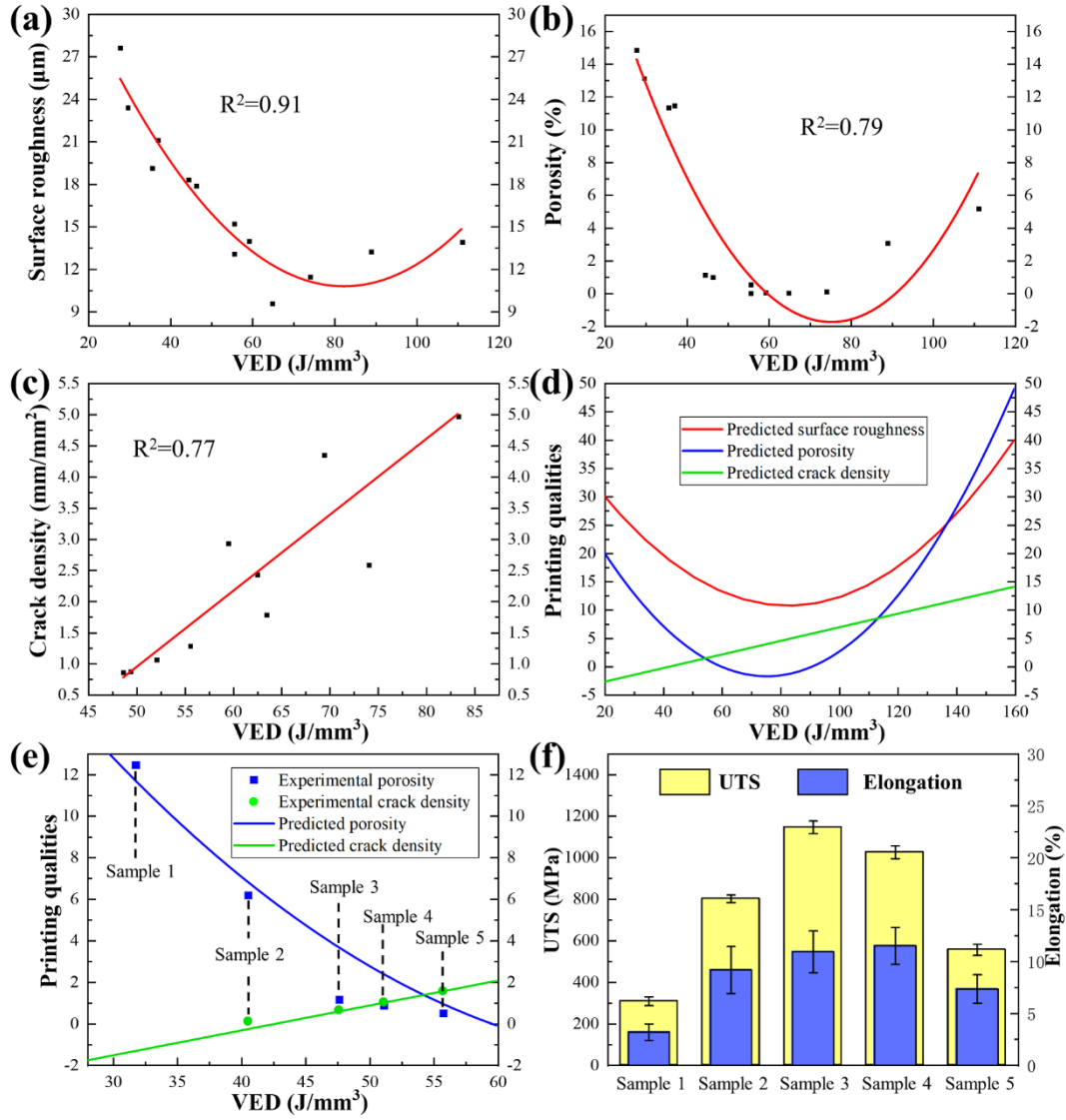


Fig. 18. Relationship between the VED and the printing quality of (a) the surface roughness, (b) the porosity and (c) the crack density by regression analysis, (d) predicted printing qualities as a function of the VED, (e) comparison between the predicted and experimental results, (f) ultimate tensile strength and elongation of the samples with different VEDs.

To further observe and analyze the morphology of the pores, CT was performed on four samples with the different VEDs. The three-dimensional (3D) reconstruction images and the size distribution of pores are shown in Fig. 19 and Fig. 20, respectively.

As shown in the reconstruction images, at a low VED of 29.63 J/mm^3 , large and irregular pores occupied the whole measured domain, indicating the occurrence of insufficient overlap, the instability of melt pool and the lack of fusion. Some pores from different layers and tracks were observed to connect with each other, accordingly forming huge hollow spaces and frame-like structures, as shown in the reconstruction image at high magnification (Fig. 19e), which corresponded to a number of pores with large size in Fig. 20a. As the VED increased to 44.44 J/mm^3 , the porosity obviously decreased to $\sim 1\%$. In this instance, a higher VED improves the printing quality drastically. That is to say, most large pores are eliminated due to the increase of the bonds between layers and tracks. With a continuous increase of the VED to 59.26 J/mm^3 , it allowed to fully melt the powders, leading to a nearly pore-free part manufactured, as shown in Fig. 19c and Fig. 20c. When the VED further increased to 88.89 J/mm^3 , round shape pores were observed scattering all over the measured domain in Fig. 19d and Fig. 19f is the view at high magnification, corresponding to the keyhole pores. The size of the keyhole pores distributed concentratedly between $15 \text{ }\mu\text{m}$ and $35 \text{ }\mu\text{m}$, as illustrated in Fig. 20d.

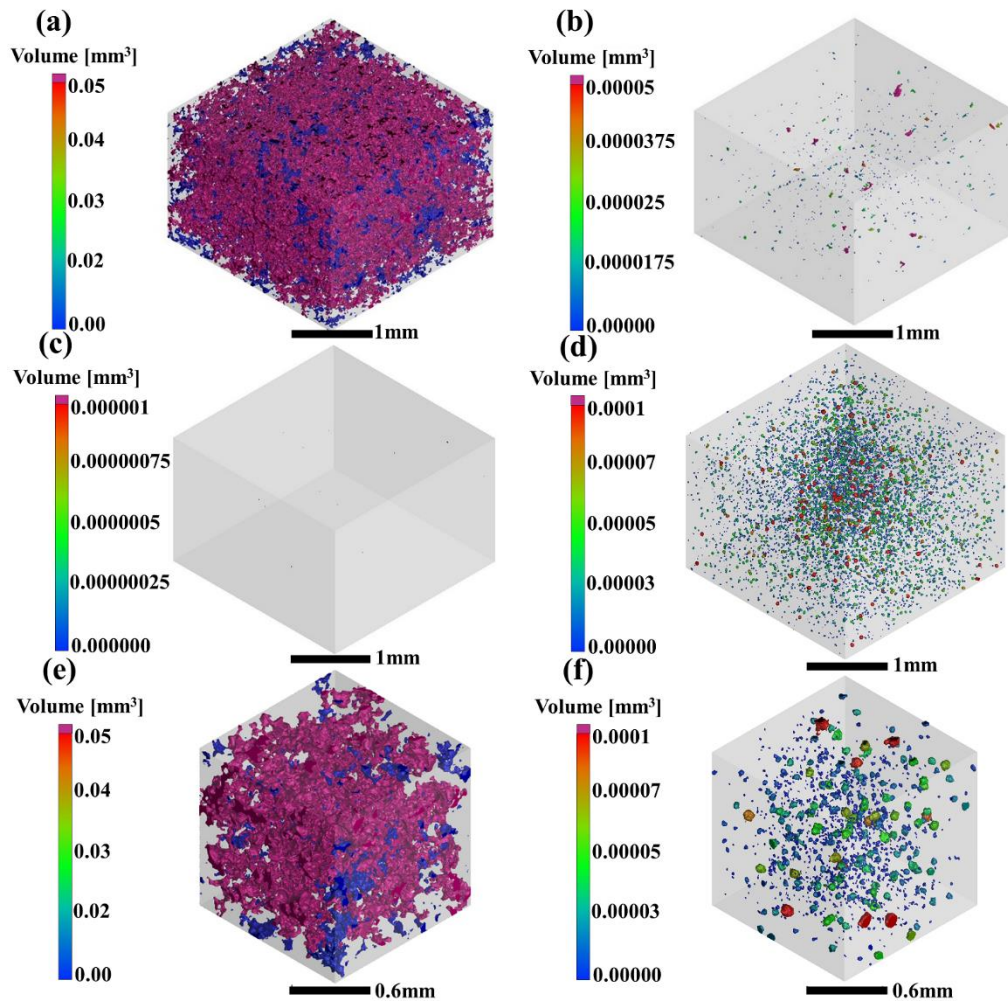


Fig. 19. 3D reconstruction of the pores at the VED of (a) 29.63 J/mm³, (b) 44.44 J/mm³, (c) 59.26 J/mm³ and (d) 88.89 J/mm³, (e) high magnification of (a), (f) high magnification of (d).

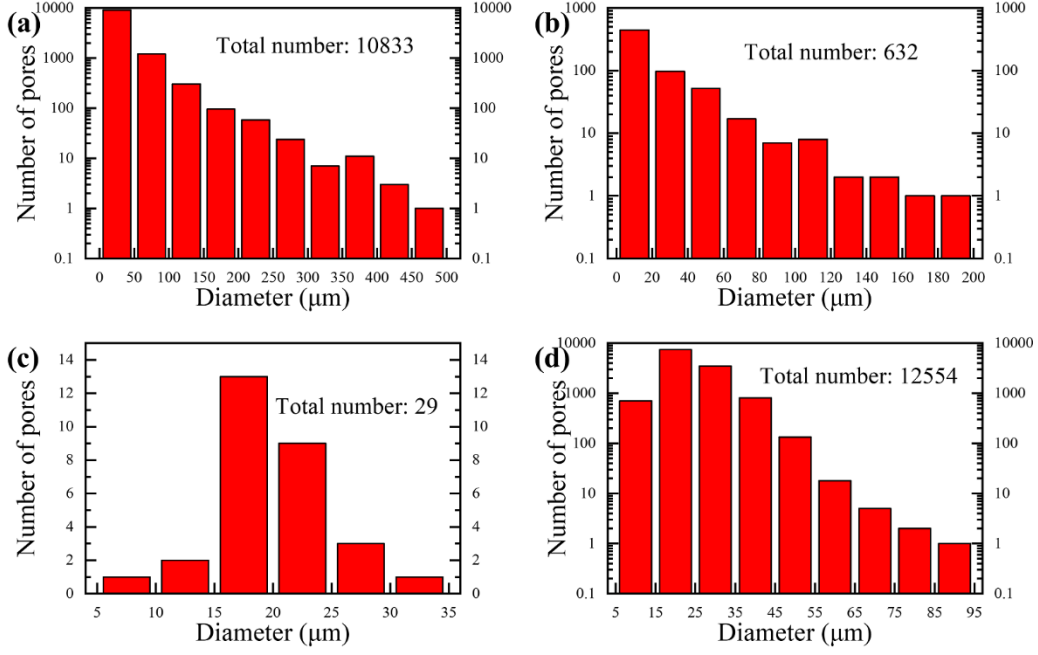


Fig. 20. Size distribution of the pores at the VEDs of (a) 29.63 J/mm³, (b) 44.44 J/mm³, (c) 59.26 J/mm³ and (d) 88.89 J/mm³.

Fig. 21 shows the distribution of the sphericity of pores. The definition of sphericity is given by Kasperovich et al. (2016) as:

$$\delta = \frac{6 \cdot \pi^{1/2} \cdot V}{A^{3/2}} \quad (3)$$

where V is the volume, and A is the surface area of the object. As δ gets closer to 1, the shape of pore gets closer to a sphere and $\delta = 1$ for a sphere. On the contrary, as δ gets smaller, the pore becomes more concave, elongated or irregular. From Fig. 21, when the VEDs were 29.63 J/mm³, 44.44 J/mm³ and 59.26 J/mm³, the sphericity mainly distributed between 0.5 and 0.7 and the corresponding frequencies were 74.11%, 81.17% and 73.53%, respectively. At a low VED of 29.63 J/mm³, the sphericity of a number of pores was lower than 0.4, implying the presence of irregular pores at such a low VED. When the VED reached 88.89 J/mm³, the sphericity of the most pores (96.99%) was larger than 0.7, indicating that the pores with a nearly round shape took the main portion

of the whole, which was consistent with the observation on metallograph and 3D CT images of the attendant keyhole pores.

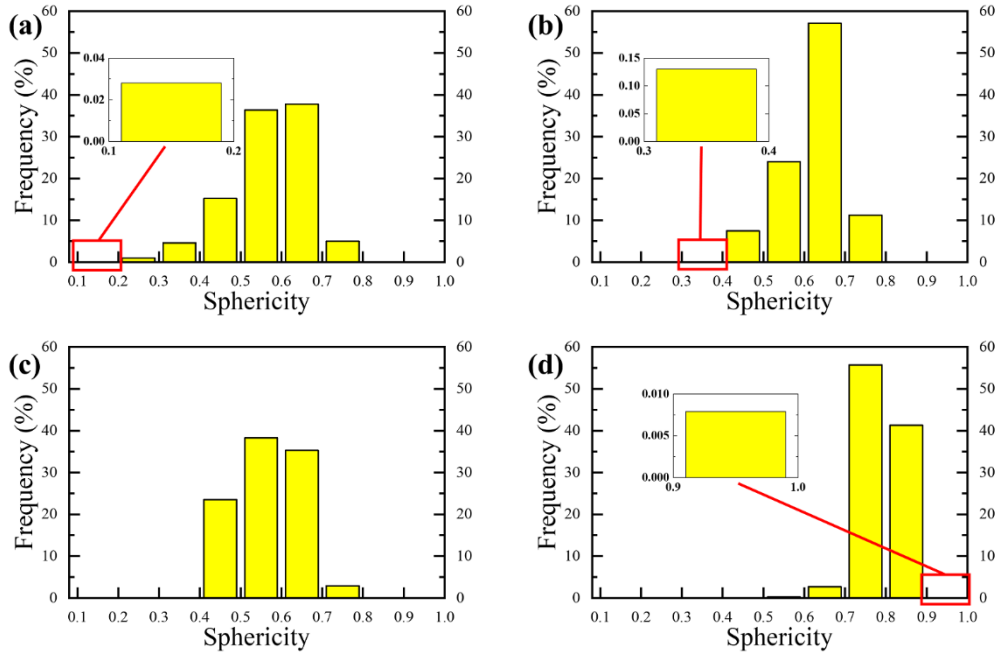


Fig. 21. Sphericity distribution of the pores at the VEDs of (a) 29.63 J/mm³, (b) 44.44 J/mm³, (c) 59.26 J/mm³ and (d) 88.89 J/mm³.

3.3. Crack

In the LPBF process, residual stress is induced by a rapid heating and cooling process. It is known as the driving force of cracking, which arises from the high thermal gradient presented in the printed part (Kruth et al. (2004)). The crack in IN738LC processed by LPBF is known as solidification crack according to the study of Cloots et al. (2016). The IN738LC alloy has a large solidification temperature range, inducing the liquid containing highly concentrated solutes to remain in the inter-dendritic regions at the last stage of solidification due to the segregation behavior. The presence of resultant liquid film leads to the weakening of grain boundaries, where cracks will occur and propagate under the thermal stress. The crack density as a function of the processing

parameters is depicted in Fig. 22.

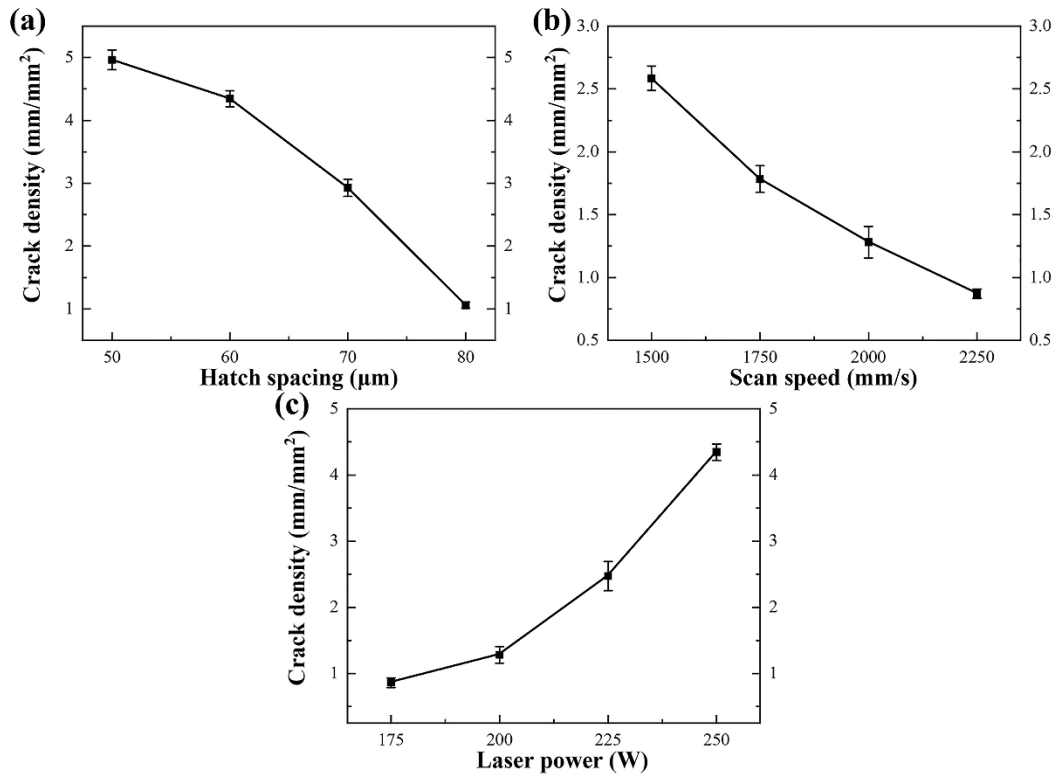


Fig. 22. Crack density as a function of (a) the hatch spacing (laser power 250 W, scan speed 2000 mm/s), (b) the scan speed (laser power 200 W, hatch spacing 60 μm) and (c) the laser power (scan speed 2000 mm/s, hatch spacing 60 μm).

3.3.1. Effect of hatch spacing

It is apparent that the crack density was inversely related to the hatch spacing, as shown in Fig. 22a. When the laser power and the scan speed were fixed, Xia et al. (2016) suggested that the decrease of the hatch spacing led to an increase of the thermal gradient between tracks, which accordingly increased the residual stress. Moreover, the low hatch spacing is favorable to increase the working temperature in melt pool, where the solidification behavior is significantly relative to the temperature of melt. The estimated time for solidification was established by Gao and Sonin (1994) as:

$$\tau = 2 \left(\frac{a^2}{3\alpha} \right) \ln \left(\frac{T_p - T_t}{T_f - T_t} \right) \quad (4)$$

where a is the radius of droplets, α is the thermal diffusivity, T_p is the peak temperature of the melting pool, T_f is the fusion temperature, and T_t is the ambient temperature. The relationship between τ and T_p is depicted in Fig. 23 as $a = 50 \mu\text{m}$, $\alpha = 4.87 \times 10^{-6} \text{ m}^2/\text{s}$, $T_t = 298 \text{ K}$ and $T_f = 1628 \text{ K}$ for IN738LC, indicating by Quested (2013). It is evident that the time for solidification is prolonged by the increase of working temperature, implying that more liquid remains between dendrites within the same amount of time for solidification. Consequently, the risk of cracking indeed increases. Therefore, more cracks were observed in the sample at a lower hatch spacing.

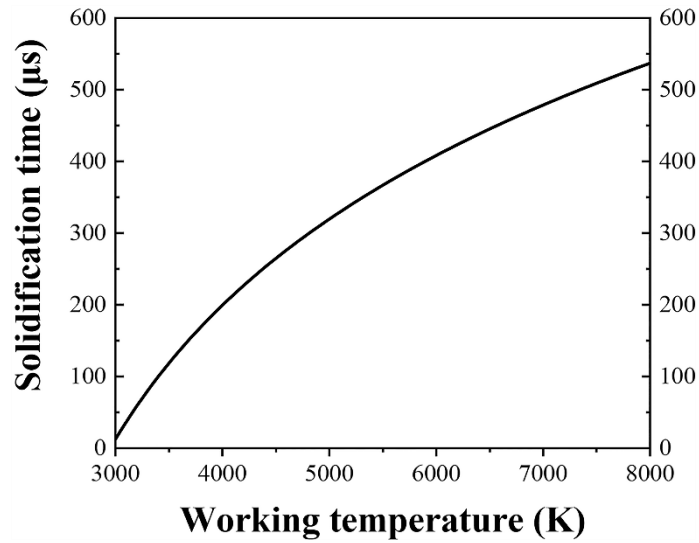


Fig. 23. Solidification time as a function of the working temperature.

3.3.2. Effect of scan speed

A subsequent decrease in the crack density with the increase of the scan speed is demonstrated in Fig. 22b. The crack density decreased from $2.59 \text{ mm}/\text{mm}^2$ to $0.87 \text{ mm}/\text{mm}^2$ as the scan speed increased from 1500 mm/s to 2250 mm/s . Xia et al. (2017) suggested that a low scan speed could increase the working temperature of the melt

pool since the energy input density increased. A higher temperature results in a considerable amount of liquid at the last stage of solidification, which is unfavorable to the crack resistance. Besides, a high scan speed implies a reduction in the time interval between tracks, which increases the re-heating frequency on the previously fabricated tracks and slows the heat transfer from the present track to solidified material, inducing a reduction in the thermal gradient and the resultant residual stress. Therefore, increasing the scan speed can effectively reduce the cracking tendency.

3.3.3. Effect of laser power

From Fig. 22c, the crack density reached its maximum value, i.e. 4.35 mm/mm^2 at the power of 250 W and successively decreased as the laser power decreased. As indicated by Li, Gu (2014) and Parimi et al. (2014), the increase of laser power is favorable for a higher thermal gradient at a given hatch spacing and scan speed, therefore, the attendant residual stress tends to increase. Besides, the increase of laser power implies more energy penetration in the powder bed and enhances thermal accumulation. Consequently, a relatively high working temperature is obtained, which accordingly induces more remaining liquid between dendrites at the last stage of solidification. Thus, a relatively high crack density tends to occur at high laser power.

3.4. Effect of VED on printing qualities

The summary of the effect of the VED on the printing qualities is depicted in Fig. 18. Fig. 18a and b show that the surface roughness and the porosity were quadratic to the VED, indicating both high and low VEDs could induce high surface roughness and porosity. The relationships can be depicted as Eq. (5) and (6), and the correlation

coefficients are $R = 0.95$ ($R^2 = 0.91$) and 0.89 ($R^2 = 0.79$), respectively. A linear relationship between the crack density and the VED shows that the crack density increased with increasing the VED, as illustrated in Fig. 18c. The corresponding fitting curve is Eq. (7) and R is 0.88 ($R^2 = 0.77$).

$$\text{Surface roughness} = 0.0049\psi^2 - 0.81\psi + 44.15 \quad (5)$$

$$\text{Porosity} = 0.0071\psi^2 - 1.07\psi + 38.52 \quad (6)$$

$$\text{Crack density} = 0.12\psi - 5.15 \quad (7)$$

In order to find the optimal VED for the fabrication of IN738LC components with high properties, the predicted results as a function of VED in terms of regression analysis are summarized in Fig. 18d. Surface roughness will not be mentioned alone in the latter part since it primarily affects the machinal performances through pores, thus the analysis of porosity has included the effect of surface roughness. According to the experimental results, the porosity reached the minimal value at the VED of ~ 55 J/mm³ and kept at this level until the VED increased to ~ 90 J/mm³ and ~ 110 J/mm³ and it rose up to 3.07% and 5.18% due to the keyhole and humping phenomena, respectively, where the crack density is predicted to continue increasing, as depicted in Fig. 18d. Therefore, the optimal properties should be obtained at the VED less than ~ 55 J/mm³. Another group of parameters was chosen randomly with the VED less than ~ 55 J/mm³ to print metallographic observation and tensile testing samples, as listed in Table 6. Fig. 18e shows a comparison between the predicted and experimental results. It is apparent that the measured crack density fixed well with the predicted curve. The trend of the measured porosity was generally consistent with the predicted

results although there were slight deviations between them. However, a large number of pores in Sample 1 made it was difficult to measure the crack density.

Sample	Laser power (W)	Scan speed (mm/s)	Hatch spacing (μm)	Volume energy density (J/mm^3)
1	200	3000	70	31.75
2	175	1800	80	40.51
3	225	1750	90	47.62
4	230	2500	60	51.11
5	250	2300	65	55.74

Table 6 Processing parameters for the analysis of the relationship between the printing qualities and the mechanical properties.

Fig. 18f shows the ultimate tensile strength (UTS) and the elongation of the testing samples with different VEDs. High porosity induced severe brittleness in Sample 1, and the UTS and the elongation were as low as 309.48 MPa and 3.21%, respectively. Both UTS and elongation of Sample 2 increased as the VED increased from 31.75 J/mm^3 to 40.51 J/mm^3 . Compared with Sample 2, the porosity decreased to 1.15% but the crack density increased to 0.65 mm/mm^2 in Sample 3. In this case, the maximum UTS (1147.26 MPa) was attained and the elongation was also improved (10.95%). A further increase in VED induced the porosity to decrease but the crack density to increase, as indicated by Fig. 18e. The elongation of Sample 4 was 11.52%, slightly higher than that of Sample 3 and dropped to 7.36% at the VED of 55.74 J/mm^3 (Sample 5). However, the UTS showed a continuous downward trend for Sample 4 (1026.98 MPa) and

Sample 5 (556.78 MPa), indicating that the mechanical properties were dominated by cracks within this VED range.

Cracks and pores can significantly affect the performances of materials related to their amount, size and morphology, etc., which need to be carefully controlled depending on the service conditions. In the current experimental condition, the VED of $\sim 48 \text{ J/mm}^3$ is optimal for IN738LC in the LPBF process. The laser power and the scan speed are considered to affect the printing qualities by a similar mechanism through the energy input. Under this VED, relatively high laser power ($\sim 300 \text{ W}$) and scan speed ($\sim 3000 \text{ mm/s}$) are not recommended due to the balling effect related to the Marangoni flow and the Plateau–Rayleigh instability. Moreover, the humping phenomenon induced by low hatch spacing ($\sim 30 \text{ }\mu\text{m}$) needs to be avoided as well.

4. Conclusion

In this study, the influence of laser power, scan speed and hatch spacing on the printing qualities including surface roughness, porosity, and crack density of IN738LC during the LPBF process were investigated. Some key findings are summarized as follow:

- Surface roughness, porosity and crack density were evidently influenced by the applied hatch spacing, scan speed and laser power in the LPBF process.
- The processes related to the solidification and fluid dynamics process such as the Marangoni convection, the micro-humping, the Plateau–Rayleigh instability, etc., were identified and characterized as the key factors that could affect the surface quality.

-
- The formation of pores was primarily attributed to the lack of fusion and the keyhole due to the different energy input densities.
 - The crack density was distinctly affected by the residual stress and the working temperature in the melt pool, which changed significantly with the process parameters.
 - The correlation between the printing qualities and the VEDs was depicted with mathematical relationships using regression analysis. According to the results of tensile testing, the VED of $\sim 48 \text{ J/mm}^3$ was found to be optimal for building IN738LC components by LPBF.

Acknowledgment

This work is financially supported by Shenzhen Science and Technology Innovation Commission under the projects (No.KQJSCX20170328155402991, No.JCYJ20170817111811303 and No.KQTD20170328154443162), National Natural Science Foundation of China (Grant No.91860131), National Key Research and Development Program of China (No.2017YFB0702901) and joint Ph.D. program between SUSTech and UoB (No.FEFE/GAS1792). Thanks are also due to Qiushuang Ge for the linear regression analysis and Guowei Ye for the measurement of crack density.

Reference

Chen Y., K. Zhang, J. Huang, S. R. E. Hosseini, Z. Li, 2016. Characterization of heat affected zone liquation cracking in laser additive manufacturing of Inconel 718. *Mater. Des.* 90, 586-594. <http://dx.doi.org/10.1016/j.matdes.2015.10.155>

-
- Cloots M., P. J. Uggowitzer, K. Wegener, 2016. Investigations on the microstructure and crack formation of IN738LC samples processed by selective laser melting using Gaussian and doughnut profiles. *Mater. Des.* 89, 770-784.
<http://dx.doi.org/10.1016/j.matdes.2015.10.027>
- Fabbro R., 2010. Melt pool and keyhole behaviour analysis for deep penetration laser welding. *Journal of Physics D: Appl. Phys.* 43(44).
<http://dx.doi.org/10.1088/0022-3727/43/44/445501>
- Gao F., Sonin Ain A., 1994. Precise deposition of molten microdrops: the physics of digital microfabrication. *Proc. R. Soc. Lond. A* 444, 533-554.
<https://doi.org/10.1098/rspa.1994.0037>
- Guo Q., Zhao C., Escano L. I., Young Z., Xiong L., Fezzaa K., Everhart W., Brown B., Sun T., Chen L., 2018. Transient dynamics of powder spattering in laser powder bed fusion additive manufacturing process revealed by in-situ high-speed high-energy x-ray imaging. *Acta Mater.* 151, 169-180.
<https://doi.org/10.1016/j.actamat.2018.03.036>
- Guraya T., S. Singamneni, Z. W. Chen, 2019. Microstructure formed during selective laser melting of IN738LC in keyhole mode. *J. Alloys Compd.* 792, 151-160.
<http://dx.doi.org/10.1016/j.jallcom.2019.03.419>
- Kasperovich G., J. Haubrich, J. Gussone, G. Requena, 2016. Correlation between porosity and processing parameters in TiAl6V4 produced by selective laser melting. *Mater. Des.* 105, 160-170.
<http://dx.doi.org/10.1016/j.matdes.2016.05.070>

-
- Khairallah S. A., A. T. Anderson, A. Rubenchik, W. E. King, 2016. Laser powder-bed fusion additive manufacturing: Physics of complex melt flow and formation mechanisms of pores, spatter, and denudation zones. *Acta Mater.* 108, 36-45.
<http://dx.doi.org/10.1016/j.actamat.2016.02.014>
- King W. E., H. D. Barth, V. M. Castillo, G. F. Gallegos, J. W. Gibbs, D. E. Hahn, C. Kamath, A. M. Rubenchik, 2014. Observation of keyhole-mode laser melting in laser powder-bed fusion additive manufacturing. *J. Mater. Process. Technol.* 214(12), 2915-2925. <http://dx.doi.org/10.1016/j.jmatprotec.2014.06.005>
- Kruth J. P., L. Froyen, J. Van Vaerenbergh, P. Mercelis, M. Rombouts, B. Lauwers, 2004. Selective laser melting of iron-based powder. *J. Mater. Process. Technol.* 149(1-3), 616-622. <http://dx.doi.org/10.1016/j.jmatprotec.2003.11.051>
- Li C., Y. B. Guo, J. B. Zhao, 2017. Interfacial phenomena and characteristics between the deposited material and substrate in selective laser melting Inconel 625. *J. Mater. Process. Technol.* 243, 269-281.
<http://dx.doi.org/10.1016/j.jmatprotec.2016.12.033>
- Li Y., D. Gu, 2014. Thermal behavior during selective laser melting of commercially pure titanium powder: Numerical simulation and experimental study. *Addit. Manuf.* 1-4, 99-109. <http://dx.doi.org/10.1016/j.addma.2014.09.001>
- Messé O. M. D. M., Muñoz-Moreno R., Illston T., Baker S., Stone H. J., 2018. Metastable carbides and their impact on recrystallisation in IN738LC processed by selective laser melting. *Addit. Manuf.* 22, 394-404.
<http://dx.doi.org/10.1016/j.addma.2018.05.030>

-
- Mumtaz K., N. Hopkinson, 2009. Top surface and side roughness of Inconel 625 parts processed using selective laser melting. *Rapid Prototyp. J.* 15(2), 96-103.
<http://dx.doi.org/10.1108/13552540910943397>
- Parimi L. L., R. G. A. D. Clark, M. M. Attallah, 2014. Microstructural and texture development in direct laser fabricated IN718. *Mater. Charact.* 89, 102-111.
<http://dx.doi.org/10.1016/j.matchar.2013.12.012>
- Qiu C., C. Panwisawas, M. Ward, H. C. Basoalto, J. W. Brooks, M. M. Attallah, 2015. On the role of melt flow into the surface structure and porosity development during selective laser melting. *Acta Mater.* 96, 72-79.
<http://dx.doi.org/10.1016/j.actamat.2015.06.004>.
- Quested P. N., R. F. Brooks, L. Chapman, R. Morrell, Y. Youssef, K. C. Mills, 2013. Measurement and estimation of thermophysical properties of nickel based superalloys. *Mater. Sci. Technol.* 25(2), 154-162.
<http://dx.doi.org/10.1179/174328408x361454>
- Rayleigh L., 2010. XVI. On the instability of a cylinder of viscous liquid under capillary force. *The London, Edinburgh, and Dublin Philosophical Magazine and Journal of Science* 34(207), 145-154. <http://dx.doi.org/10.1080/14786449208620301>
- Rombouts M., J. P. Kruth, L. Froyen, P. Mercelis, 2006. Fundamentals of Selective Laser Melting of alloyed steel powders. *CIRP Annals* 55(1), 187-192.
[http://dx.doi.org/10.1016/s0007-8506\(07\)60395-3](http://dx.doi.org/10.1016/s0007-8506(07)60395-3)
- Scipioni Bertoli U., A. J. Wolfer, M. J. Matthews, J.-P. R. Delplanque, J. M. Schoenung, 2017. On the limitations of Volumetric Energy Density as a design parameter for

-
- Selective Laser Melting. Mater. Des. 113, 331-340.
<http://dx.doi.org/10.1016/j.matdes.2016.10.037>
- Tan C., K. Zhou, W. Ma, L. Min, 2018. Interfacial characteristic and mechanical performance of maraging steel-copper functional bimetal produced by selective laser melting based hybrid manufacture. Mater. Des. 155, 77-85.
<http://dx.doi.org/10.1016/j.matdes.2018.05.064>
- Tian Y., D. Tomus, P. Rometsch, X. Wu, 2017. Influences of processing parameters on surface roughness of Hastelloy X produced by selective laser melting. Addit. Manuf. 13, 103-112. <http://dx.doi.org/10.1016/j.addma.2016.10.010>
- Wang H., Zhang X., Wang G. B., Shen J., Zhang G. Q., Li Y. P., Yan, M., 2019. Selective laser melting of the hard-to-weld IN738LC superalloy: Efforts to mitigate defects and the resultant microstructural and mechanical properties. J. Alloys Compd. 807.
<http://dx.doi.org/10.1016/j.jallcom.2019.151662>
- Xia M., D. Gu, G. Yu, D. Dai, H. Chen, Q. Shi, 2016. Influence of hatch spacing on heat and mass transfer, thermodynamics and laser processability during additive manufacturing of Inconel 718 alloy. Int. J. Mach. Tool. Manu. 109, 147-157.
<http://dx.doi.org/10.1016/j.ijmachtools.2016.07.010>
- Xia M., D. Gu, G. Yu, D. Dai, H. Chen, Q. Shi, 2017. Porosity evolution and its thermodynamic mechanism of randomly packed powder-bed during selective laser melting of Inconel 718 alloy. Int. J. Mach. Tool. Manu. 116, 96-106.
<http://dx.doi.org/10.1016/j.ijmachtools.2017.01.005>
- Yadroitsev I., A. Gusarov, I. Yadroitsava, I. Smurov, 2010. Single track formation in

selective laser melting of metal powders. J. Mater. Process. Technol. 210(12),
1624-1631. <http://dx.doi.org/10.1016/j.jmatprotec.2010.05.010>

Zhou X., X. Liu, D. Zhang, Z. Shen, W. Liu, 2015. Balling phenomena in selective laser
melted tungsten. J. Mater. Process. Technol. 222, 33-42.
<http://dx.doi.org/10.1016/j.jmatprotec.2015.02.032>